



Compact, tunable microring resonator on a lithium niobate platform using etchless fabrication methods

ADNAN GHUMRO,^{1,*}  JACK A. SMITH,¹  LOYD J. MCKNIGHT,^{1,2}
AND MICHAEL J. STRAIN¹ 

¹*Institute of Photonics, Dept. of Physics, University of Strathclyde, Technology and Innovation Centre, 99 George St., Glasgow G1 1RD, UK*

²*Fraunhofer Centre for Applied Photonics, Technology and Innovation Centre, 99 George St., Glasgow G1 1RD, UK*

*adnan@strath.ac.uk

Abstract: Tunable microring resonators on a lithium niobate on insulator (LNOI) platform are demonstrated, making use of thick polymer strip-loaded waveguides and bound states in the continuum (BIC) to achieve compact devices without plasma etching. The racetrack resonator device, with a bend radius of $94\ \mu\text{m}$, demonstrates strong confinement for TM-polarized modes, enabling electro-optic modulation with a modest half-wave voltage–length product of $35\ \text{Vcm}$. The device achieves a loaded quality factor of 4.17×10^4 for TM polarization and also supports purely linear TE modes with a loaded quality factor of 1.1×10^4 through guiding in the polymer layer. This etch-free process simplifies fabrication while maintaining access to lithium niobate's $\chi^{(2)}$ nonlinearity, offering a scalable route for photonic integrated circuits that combine reduced footprint, effective electro-optic performance with future potential for polarisation diversity on-chip.

Published by Optica Publishing Group under the terms of the [Creative Commons Attribution 4.0 License](https://creativecommons.org/licenses/by/4.0/). Further distribution of this work must maintain attribution to the author(s) and the published article's title, journal citation, and DOI.

1. Introduction

Electro-optic (EO) modulators are crucial components in photonic integrated circuits (PICs), enabling the conversion of electrical signals into the optical domain for high speed communication [1], data centers [2], and emerging applications including quantum information processing, switching [3,4], and optical neural networks [5]. In addition to modulation functionality, practical photonic integrated circuits rely on active tunability to achieve reconfigurability [6], precise resonance alignment, and compensation for fabrication-induced variations [7]. Among the several material platforms available, lithium niobate has emerged as an excellent candidate due to its strong Pockels effect, low propagation losses, and wide transparency. Recent advancement in thin film lithium niobate on insulator (LNOI) have led to the demonstration of EO modulators with high bandwidths and low driving voltages [8–10].

Several approaches have been used to realise efficient EO modulators on a LN platform. Monolithic LN devices, where waveguides are fully or partially etched into the thin film, exhibit exceptional performance with high quality factors microrings ($>10^6$), and low propagation loss [11–13]. However, the material is difficult to etch and the fabrication of waveguides relies on the transfer of a lithographic mask into the LN material via inductively coupled plasma-reactive ion etching (ICP-RIE), which must be optimised for line-edge smoothness to minimise scattering losses [8,14]. The LN etch process is generally considered as incompatible with other material platforms sharing toolsets due to contamination of the process chamber that can detrimentally affect subsequent processing [15]. The heterogeneous integration of lithium niobate (LN) with

silicon, achieved through either transfer printing [16–19] or thin-film bonding [20,21], offers an alternative pathway for realizing electro-optic (EO) modulators. This approach enables LN to be incorporated as a back-end process within silicon photonics, thereby enhancing the platform with high-performance EO functionality while retaining access to well-established silicon photonics design libraries. In transfer-printed devices, the hybrid integration process typically requires additional fabrication steps for membrane release, alignment, and bonding, and the lithium niobate membranes often need to be etched to define the waveguide structures, resulting in increased process complexity.

As an alternative to etched waveguides, there have been a number of demonstrations of strip-loaded waveguiding on the LNOI platform utilizing SiN [22–26], Si [27,28], TiO₂ [29,30], and chalcogenide glass [31]. By patterning dielectric or polymer strips onto the LNOI, optical modes can be guided via effective refractive-index effects, with optical confinement to the LN material maximised through the use of low refractive index strip materials [32]. Although an etch-free process, strip loaded waveguides are typically weakly guiding, leading to prohibitive radiative bend losses for radii below the few hundred micron range. Although this is sufficient for long propagation length interferometric modulator geometries, it is prohibitive for production of compact optical devices on-chip. To overcome these limitations, bound states in the continuum (BIC) have recently been explored as a mechanism to enhance optical confinement in dielectric waveguides [33]. BIC modes enable strong localisation of light within a waveguide without introducing significant radiation losses, thereby allowing strip-loaded structures to achieve compact devices similar to that of fully etched counterparts while retaining fabrication simplicity with recent demonstration of micro-resonators and modulators [33–35].

BIC modes can occur in optical waveguides, where they appear as guided modes that do not couple to the surrounding radiation modes [34,36]. They originate from quasi-TM leaky modes that would normally lose energy through lateral leakage; but under certain conditions, this loss can be suppressed by engineering the destructive interference of those leaky modes [37,38]. In our case, a standard strip-loaded waveguide configuration consisting of low-index polymer patterned on top of the high-index lithium niobate can be made to support bound in continuum modes through careful selection of the polymer width and radius. For certain widths and radii, the BIC mode will stay laterally confined within the high refractive index lithium niobate, even for radii well below the cut-off radius for conventional strip-loaded waveguides. This provides an etch-free alternative to fabricating tightly confining lithium niobate devices.

Table 1 summarizes the key characteristics of various lithium niobate (LN) platforms employed for electro-optic (EO) resonant modulators. Monolithic LN modulators offer the highest EO performance but are limited by aggressive fabrication processes. Transfer-printed devices, while enabling heterogeneous integration, require LN etching and an additional transfer step, which can increase process complexity. Strip-loaded platforms provide a good balance between EO performance and fabrication simplicity but typically exhibit larger bend radii. The strip loaded BIC approach offers reduced bend radius and simplified fabrication with low loss. We demonstrate the smallest active BIC-based resonator with simple fabrication process, and adequate EO performance compared to other LN platforms.

In this work, we harness BICs in strip-loaded lithium niobate waveguides to design and fabricate a BIC-based active ring modulator featuring bend radii of just 94 μm . The proposed approach combines the practical advantages of strip-loaded while substantially reducing the footprint. Experimentally, we demonstrate a maximum loaded quality factor of $Q_{\text{loaded}} = 4.17 \times 10^4$ (TM polarization) and a half-wave voltage–length product of $V_{\pi}L = 35 \text{ V cm}$.

Table 1. Comparison of lithium niobate platforms for electro-optic modulators

Platform	Device	Material	Bend Radius	Propagation Loss (dB/cm)	Fiber-Chip Loss (dB)	Additional Loss (dB)	Total Loss (dB)	Fabrication Requirements	EO Coeff.	$V_{\pi} L$ (Vcm)	Tunability (pm/V)
Monolithic ^a [11]	Microring	X-cut	80 μm	0.093	–	–	>0.093	LN etching	N/A	N/A	N/A
Monolithic [10]	Racetrack / MZI	X-cut	–	3	10	N/A	>13	LN etching	r_{33}	–7	1.8/–
Transfer Printing ^a [17]	Microring	Z-cut	40 μm	3	–	–	>3	SiN and LN etching	N/A	N/A	N/A
Transfer Printing [18]	Microring	X-cut	100 μm	–	4	–	>4	SiN and LN etching	r_{33}	–	1.7 ^b
Transfer Printing [39]	MZI	X-cut	–	–	18	3.3	>21	SiN and LN etching	r_{33}	6 ^b	–
Strip-loaded [22]	Microring	X-cut	300 μm	0.32	–	–	>0.32	SiN etching	r_{33}	–	1.78
Strip-loaded [25]	Racetrack	X-cut	300 μm	0.2	12.8	N/A	13	SiN etching	r_{33}	5.1	2.9
Strip-loaded [26]	MZI	X-cut	300 μm	–	13.6	5.4	19	SiN etching	r_{33}	2.1	–
Strip-loaded BIC [33,40]	Microring ^a /MZI	Z-cut	~ 100 μm	1.5	20	N/A	>21	Non-etched	r_{51}	N/A /80	N/A /–
This Work	Racetrack	X-cut	94 μm	2^c	4^c	N/A	6	Non-etched	r_{13}	35	0.49

^aIndicates a passive device (no active modulation demonstrated).

^bIndicates data for single-arm measurement.

^cIndicates that the value is estimated from insertion loss measurement.

– Indicates that data is not reported in papers.

2. Mode simulations and bend losses

When designing polymer strip-loaded structures on lithium niobate (LN), two primary factors must be considered. First, the mode overlap with LN, denoted as Γ_{LN} , should be maximized to enhance nonlinear performance. Second, bend losses must be minimized to enable compact device layouts, such as ring resonators. We carried out Finite-Difference Time-Domain (FDTD) simulations of strip-loaded waveguides using the commercial solver Tidy3D [41]. An SU-8 layer with a thickness of 2 μm on 300 nm thick LN was employed in the simulations. Waveguide widths were varied from 1 to 4.5 μm in 100 nm step size, as shown in Fig. 2(a,b) for the transverse electric (TE) and transverse magnetic (TM) modes, respectively. For waveguide bends, the bend radius was varied from 40 and 121 μm with 3 μm step size as shown in Fig. 2(d,e) for TE and TM, respectively. As illustrated in Fig. 1(a), the TE mode is predominantly confined in the LN layer. Its loss increases gradually with waveguide width, though the absolute loss remains small. By contrast, the TM mode exhibits sharp reductions in loss at specific widths, corresponding to conditions where the TM mode transitions into a bound state by decoupling from the TE continuum as shown in Fig. 2(b). This phenomenon corresponds to the formation of a BIC, and the mode profile of BIC mode is shown in Fig. 1(b). Wider waveguides also exhibit low TM loss due to weak coupling to the TE continuum, though this comes at the cost of reduced optical confinement. Figure 2(c) presents the loss for TE and TM at 1550 nm, TE losses remain <1 dB/cm for all simulated widths, but the TM mode has low loss at ~ 2 and 4 μm waveguide widths. Importantly, the tolerance for maintaining low loss, on the order of 2 dB/cm, spans nearly 400 nm which is readily attainable with standard nanofabrication processes. For photonic components such as ring resonators, waveguide bends play a critical role. Similar to straight sections, the interaction between the bound TM mode and the TE continuum depends on resonant mode coupling as a function of cross-sectional geometry, but in this case is additionally influenced by the bend radius [33]. Figure 2(d) shows that the TE mode behaves like a conventional guided mode, with bend loss decreasing exponentially, and achieves low loss for radii of several hundreds of microns. In contrast, the TM mode exhibits distinct regions of suppressed bend loss, as illustrated in Fig. 2(e) where losses can fall below 5 dB/cm. The electric field distribution in dB of the circular bend at 100 μm is shown in Fig. 2(h). In this case, destructive interference occurs between the TM leaky mode and the TE continuum, resulting in light confinement within the bend, thereby forming a BIC mode. In contrast, Fig. 2(i) illustrates the non-BIC regime,

where destructive interference does not occur, leading to light leakage from the bend. Figure 2(f) presents the bend loss for waveguide widths of 2 and 3 μm at $\lambda = 1550\text{ nm}$ for both TE and TM modes. For both waveguide widths, the TE modes show an exponential decrease in bend loss, consistent with the conventional behavior of bent waveguides, whereas the TM modes show sharp reductions in loss at specific radii, corresponding to the fulfillment of the BIC condition. Notably, the 2 μm waveguide bend exhibits shallower transitions compared to the 3 μm case, where the difference between the low-loss and high-loss peaks spans nearly three orders of magnitude. This stronger contrast in the 3 μm waveguide width arises from its higher propagation loss in the straight section. Therefore, careful selection of the straight waveguide width is essential to achieve relatively low bend losses. For instance, the 2 μm waveguide maintains losses below 7 dB/cm over a bend radius range from approximately 70 μm to 120 μm , with a minimum loss of $\sim 5\text{ dB/cm}$ and Fig. 2(g) presents the zoomed view bend loss of TM mode for both waveguides. The optical loss in straight waveguides has contributions from scattering and radiation losses resulting from mode overlap of the guided modes with the sidewall roughness of the SU8 rib structure, in addition to the coupling between the bound guided mode and the continuum of radiative modes in BIC guiding conditions [33]. In practical applications, the sensitivity of the BIC condition to geometric variations leads to residual radiation loss, such that the minimum achievable propagation loss is determined by fabrication tolerances and residual leakage.

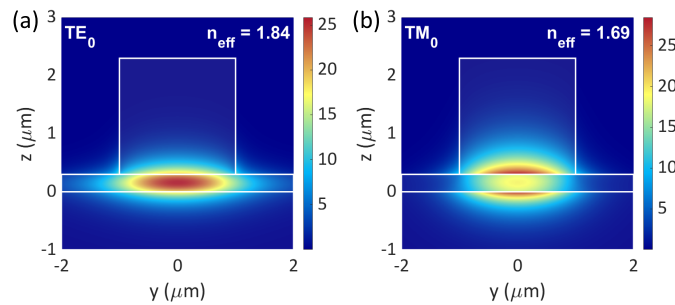


Fig. 1. Mode profiles of strip-loaded waveguides at $\lambda = 1.55\ \mu\text{m}$ (a) TE mode, (b) TM bound mode, where the waveguide dimensions are 2 μm by 2 μm , and lithium niobate slab thickness is 300 nm. n_{eff} : effective index of the mode

For EO modulation, Mach–Zehnder interferometer (MZI) configurations are widely used due to their ability to support high modulation bandwidths. However, achieving lower driving voltages typically requires longer interaction lengths, leading to a trade-off between device performance and compactness. In contrast, ring-resonator-based modulators exploit resonant enhancement to enable strong EO modulation within a significantly reduced footprint at the expense of optical bandwidth. In this work, we utilize a ring resonator with a bend radius of 94 μm and a waveguide width of 2 μm , parameters at which a BIC is formed, thereby minimizing propagation losses.

3. Fabrication of polymer strip loaded microracetrack resonator

A fabrication process for etch-less micro ring resonator used 300 nm x-cut lithium niobate ((Fig. 3(a)). SU8 polymer resist was utilized as the strip material. A 2 μm layer of SU8 6002 resist was spin coated on the LNOI sample(Fig. 3(b)) and direct write laser lithography (Heidelberg DWL66+) was used to define the strip-loaded waveguide patterns(Fig. 3(c)). Metal contact regions were defined using a lift-off process and metal evaporation of a bilayer of 50 nm : 200 nm Ti: Au (Fig. 3(d)). Waveguides were designed as facet coupled devices using a cleaved end-facet process. The optical microscope images of straight waveguides and ring resonator are shown in Fig. 3(e) and (f), respectively. A bend radius of 94 μm was identified as the minimum

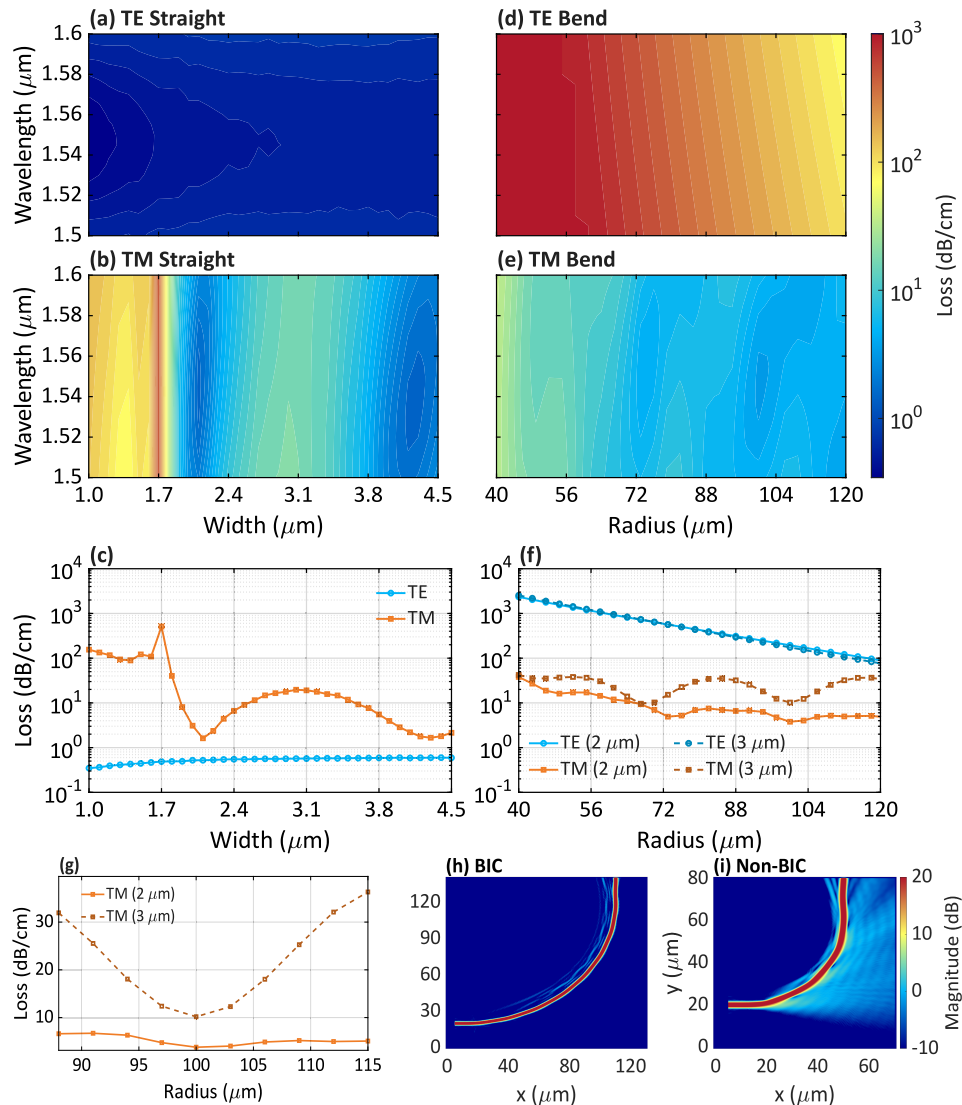


Fig. 2. FDTD simulations of a strip-loaded waveguide performed with Tidy3D [41]. (a) and (b) show the wavelength-dependent propagation loss of straight waveguides with widths from 1.0 to 4.5 μm for the TE and TM modes, respectively. (c) plots the straight-waveguide loss at $\lambda = 1.55 \mu\text{m}$ for both modes. (d) and (e) present the bend loss of a 90° circular bend (waveguide width 2 μm) for radii ranging from 40 to 121 μm with 3 μm step size, for TE and TM, respectively. (f) shows the bend loss at $\lambda = 1.55 \mu\text{m}$ versus bend radius for the two modes at 2 and 3 μm waveguide width. (g) Zoomed view of (f) comparing TM mode bend loss for waveguide widths of 2 and 3 μm . The legend indicates 2 and 3 μm waveguide widths for both TE and TM bends. Electric field magnitude (in dB) for circular bends in two configurations: (h) BIC mode with a radius of 100 μm , and (i) non-BIC mode with a radius of 40 μm .

bend loss experimentally from s-bend waveguide measurements of devices with varying radius, with deviation from simulation results likely due to differences in material refractive index as compared to simulated values. We used Euler bends following the formulation in [42] to

minimize the modal mismatch between straight and curved section. The Euler section covers an angular fraction $p\alpha/2$ of the total bend angle α , where p denotes the bend parameter. The arc length at which the Euler section transitions to the constant-curvature circular arc is given by $s_p = R_0\sqrt{p\alpha/2}$, and the corresponding transition radius $R_p = 1/\kappa(s_p)$ where the curvature of the Euler is defined as $\kappa(s_p) = 2s_p/R_0^2$. In our implementation, $\alpha = \pi$, the bend parameter was $p = 0.3$, and the effective bend radius was $R_{\text{eff}} = 94 \mu\text{m}$. The resonator design uses an evanescent field coupler with a coupling gap of $0.75 \mu\text{m}$, a coupling length of $100 \mu\text{m}$, and a phase modulation section comprising straight waveguides of lengths 1 mm and 2.5 mm . The electrodes are positioned with a $5 \mu\text{m}$ gap, centered on the strip waveguide.

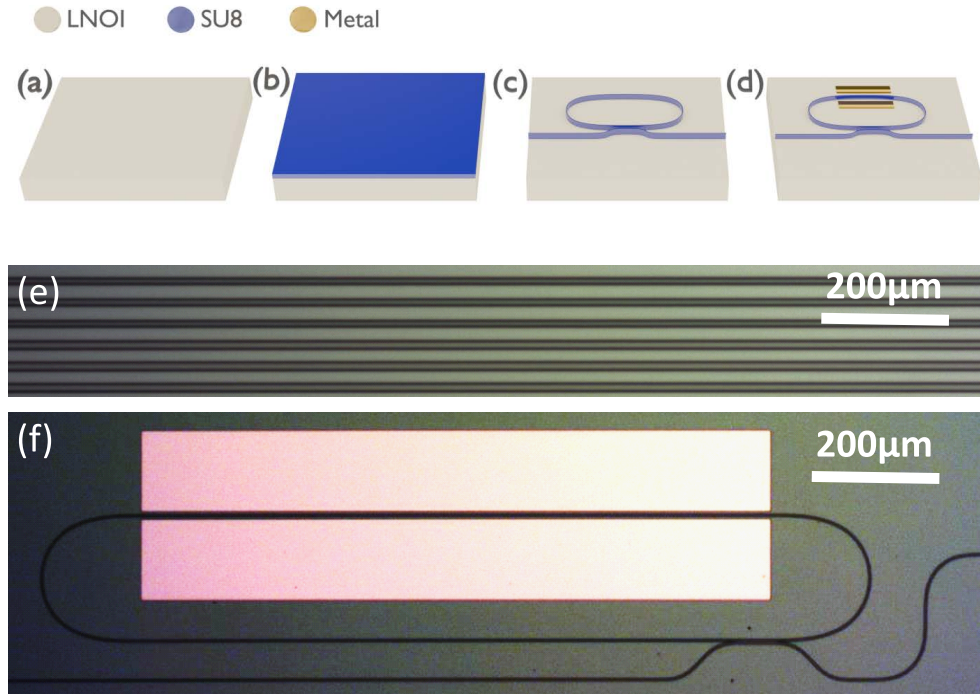


Fig. 3. Fabrication process for strip-loaded waveguides. (a) 300 nm-thick X-cut LNOI sample. (b) Spin-coating of SU-8 on the LNOI substrate. (c) Photolithography to define the strip-loaded waveguide patterns. (d) Metal deposition to form electrodes. Optical micrographs of the fabricated devices: (e) straight waveguides and (f) a micro-racetrack resonator with electrodes.

4. Optical transmission

The strip-loaded racetrack device was characterized using an end-fire optical injection setup, as illustrated in Fig. 4. The optical setup includes a tunable laser source (Agilent 8164B) connected to an optical isolator, which is subsequently linked to a polarization-maintaining lensed fibre used to inject the light onto the chip. The light transmitted through the waveguide was collected by an objective lens, followed by a polarization beam splitter (PBS), and then focused onto a free-space photodetector (Thorlabs PDA20C/M). For active measurements, a 20 MHz function generator (Aim-TTi TG120) was utilized to supply $20 V_{\text{pp}}$ sine wave to perform the amplitude modulation of the racetrack. The insertion loss for straight waveguide with a width of $2 \mu\text{m}$ is $\sim 5 \text{ dB}$ ($\sim 6 \text{ dB}$) for the TE(TM) polarization. Insertion loss measurements on cutback waveguides were carried out to allow differentiation between fiber-chip and propagation losses. Propagation losses extracted

for the TE(TM) polarizations were $1(2)\text{dBcm}^{-1}$ respectively and fiber-chip coupling losses were measured at 2dB per facet.

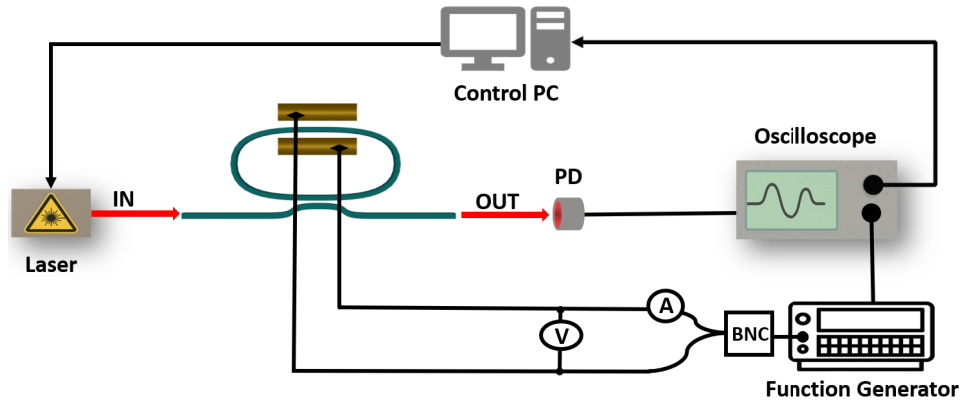


Fig. 4. Optical transmission measurement setup for racetrack characterization. For electro-optic measurements, a 20 MHz function generator supplies a sinusoidal drive signal to the device under test. PD: photodetector.

The optical transmission spectra of the strip-loaded racetrack resonators fabricated on 300 nm X-cut lithium niobate with a bend radius of $94\ \mu\text{m}$ are presented in Fig. 5. For TM polarization, the resonator exhibits a free spectral range (FSR) of 0.43 nm and fitted Q-factor(FWHM) of 3.18×10^4 ($49.9\ \text{pm}$) at the resonance wavelength $\lambda = 1588.27\ \text{nm}$, as shown in Fig. 5(a) and (b). Interestingly we observed that the racetrack guides light for TE mode polarization as depicted in Fig. 5(c) and (d) presents the associated fitted Q-factor. The measured FSR is $0.54\ \text{nm}$ and fitted Q-factor(FWHM) of 1.18×10^4 ($134.7\ \text{pm}$) at resonance $\lambda = 1588.27\ \text{nm}$. As discussed in the mode simulation, the fundamental TE mode suffers from considerable bending loss, estimated at approximately 500 dB/cm for a bend radius of $94\ \mu\text{m}$. Despite these significant losses, the strip-loaded structure continues to guide light effectively under TE excitation. Mode profiles (see Fig. 6) indicate that the waveguide supports another mode mainly confined to the SU8 in both the straight and curved sections. The group index n_g extracted from the FSR and the equation $n_g = \lambda^2 / (\text{FSR} \cdot L)$ [Fig. 5(e)] closely matches that of the SU-8 mode obtained from simulations, confirming that the guided TE mode primarily resides in the SU-8 layer rather than in the lithium niobate. Conversely, the n_g derived from TM mode measurements suggests confinement within the lithium niobate core, confirming that the TM mode remains guided in the LN layer. Mode converters could be employed in future designs to efficiently transition the SU-8 TE mode in the curved sections into the LN TE mode in the straight regions, thereby enabling electro-optic modulation through stronger tensor components in strip-loaded devices.

5. Active modulation

For active modulation, we used a racetrack with $2.5\ \text{mm}$ straight waveguide length. The transmission spectrum of the device is presented in Fig. 7(a) and associated fitted Q-factor in Fig. 7(b). The measured FSR is $0.21\ \text{nm}$ and fitted Q-factor(FWHM) of 4.17×10^4 ($38.06\ \text{pm}$) at resonance $\lambda = 1588.3\ \text{nm}$. For EO modulation, the laser was parked at the quadrature point of the resonance. The schematic shown in Fig. 4 was used, where the racetrack resonator is supplied with $20\ \text{V}_{\text{pp}}$ using function generator. An amplitude modulation depth of 3 dB was measured, corresponding to a half-wave voltage-length product of $V_{\pi}L = 35\ \text{V} \cdot \text{cm}$ for a racetrack resonator with an electrode length of 2.5 mm. The device exhibited a wavelength tunability of $0.49\ \text{pm}\ \text{V}^{-1}$ for a same electrode length as shown Fig. 7(c), which is approximately

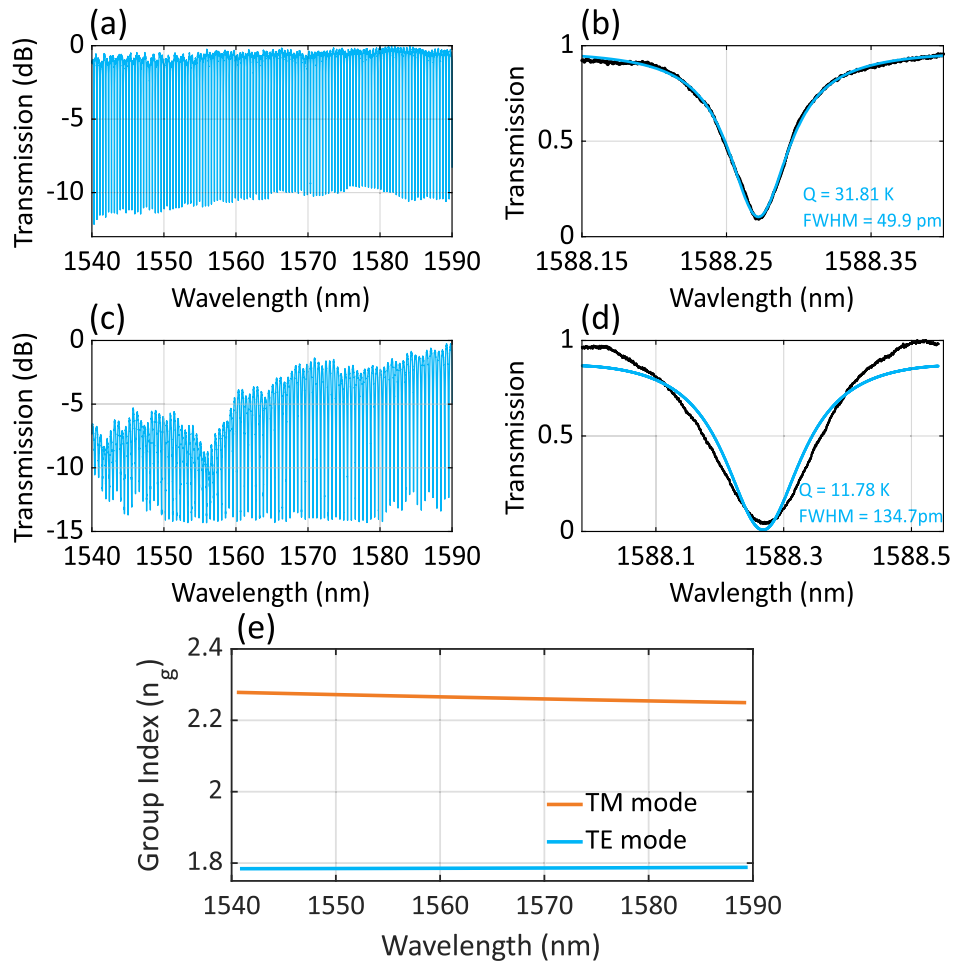


Fig. 5. TM and TE mode transmission spectra of strip-loaded micro-racetrack resonators. (a) and (c) show the measured transmission for TM and TE polarizations, respectively, for a racetrack with a 1.0 mm straight waveguide section. (b) and (d) show the associated fitted resonances at $\lambda = 1588.27$ nm. (e) shows the group index for both TE and TM mode polarization. Here Q denotes the loaded quality factor and FWHM the full width at half maximum.

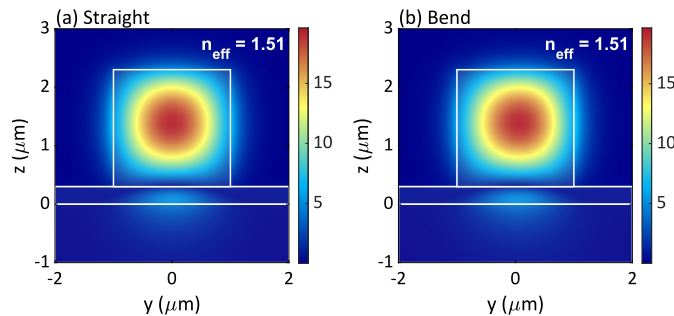


Fig. 6. TE mode profiles of the polymer waveguide mode at $\lambda = 1.55$ μm . (a) Straight waveguide; (b) bend waveguide with radius 94 μm . n_{eff} : effective index of the mode.

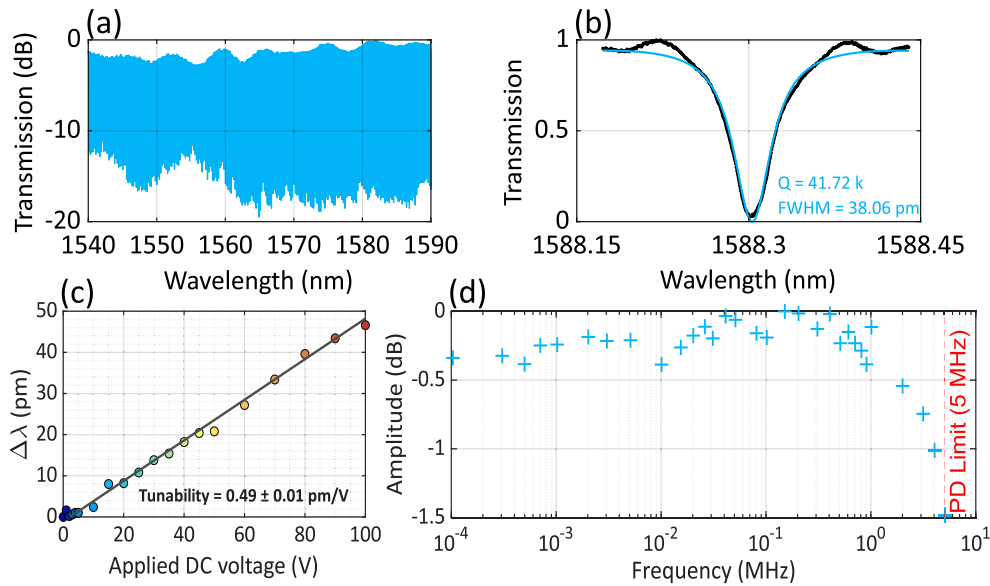


Fig. 7. Transmission spectrum of the strip-loaded racetrack resonator with a 2.5 mm electrode length for TM polarization is shown in (a), while the corresponding fitted resonance at $\lambda = 1588.3$ nm is presented in (b). (c) shows the DC tuning curve of the racetrack resonator. A linear fit yields a tunability of 0.49 ± 0.001 pm/V (d) presents the normalized amplitude response of the racetrack resonator under a 20 V_{pp} sinusoidal drive, with the laser wavelength parked at the quadrature point of the resonance ($\lambda = 1588.29$ nm). PD: Photodetector.

three times lower than fabricated using transfer print integration of a LN film on a SiN waveguide. This difference is consistent with the fact that our device operates with TM polarization, whereas [18] design employs TE polarization, which exhibits an electro-optic coefficient nearly three times larger. Although presenting a lower tuning efficiency our device benefits from extremely simple fabrication process and low insertion loss, dominated by chip-fibre transitions. The electro-optic response of the racetrack is shown in Fig. 7(d). The device exhibits a satisfactory performance over the range of applied frequencies before reaching photodetector bandwidth limit of 5 MHz. We attempted to tune the resonator under TE polarization; however, no effective tuning was observed. This can be attributed to the fact that a significant portion of the mode field is confined within the SU-8 layer, which lacks a second order nonlinearity ($\chi^{(2)}$).

6. Conclusion

We have demonstrated a compact and tunable strip-loaded lithium niobate racetrack resonator exploiting bound states in the continuum. The device leverages an etchless fabrication process that avoids plasma dry-etching of lithium niobate while still enabling efficient electro-optic modulation. Amplitude tuning was observed exclusively for TM modes, with the resonator achieving a maximum loaded quality factor of $Q_{\text{loaded}} = 4.17 \times 10^4$ and a half-wave voltage-length product of $V_{\pi}L = 35$ V cm. Although the racetrack geometry also supports TE modes, they exhibit a lower quality factor ($Q_{\text{loaded}} = 1.70 \times 10^4$) and no measurable electro-optic tuning, as this suggest the field predominantly confined within the SU-8 layer. These results highlight the potential of strip-loaded resonators as a promising platform for applications that demand simple fabrication yet effective performance, and further underline the advantages of BIC-enabled mode control in lithium niobate photonics.

Funding. Engineering and Physical Sciences Research Council (EP/V004859/1); Fraunhofer UK Research; Royal Academy of Engineering (Research Chairs and Senior Research fellowships).

Acknowledgment. This work was supported by the Engineering and Physical Sciences Research Council (EP/V004859/1), Fraunhofer UK and the Royal Academy of Engineering, Research Chairs and Senior Research Fellowships.

Disclosures. All authors declare no conflict of interest.

Data availability. Data underlying the results presented in this paper are not publicly available at this time but may be obtained from the authors upon reasonable request.

References

1. P. J. Winzer, D. T. Neilson, and A. R. Chraplyvy, "Fiber-optic transmission and networking: the previous 20 and the next 20 years [Invited]," *Opt. Express* **26**(18), 24190 (2018).
2. A. H. Atabaki, S. Moazeni, F. Pavanello, *et al.*, "Integrating photonics with silicon nanoelectronics for the next generation of systems on a chip," *Nature* **556**(7701), 349–354 (2018).
3. H.-P. Lo, T. Ikuta, N. Matsuda, *et al.*, "Electro-optic modulators for photonic quantum information processing," in *Quantum and Nonlinear Optics VI*, Q. Gong, G.-C. Guo, and B.-S. Ham, eds. (SPIE, Hangzhou, China, 2019), p. 24.
4. M. Gimeno-Segovia, H. Cable, G. J. Mendoza, *et al.*, "Relative multiplexing for minimising switching in linear-optical quantum computing," *New J. Phys.* **19**(6), 063013 (2017).
5. R. Hamerly, L. Bernstein, A. Sludds, *et al.*, "Large-Scale Optical Neural Networks Based on Photoelectric Multiplication," *Phys. Rev. X* **9**(2), 021032 (2019).
6. W. Bogaerts, D. Pérez, J. Capmany, *et al.*, "Programmable photonic circuits," *Nature* **586**(7828), 207–216 (2020).
7. W. A. Zortman, D. C. Trotter, and M. R. Watts, "Silicon photonics manufacturing," *Opt. Express* **18**(23), 23598 (2010).
8. D. Zhu, L. Shao, M. Yu, *et al.*, "Integrated photonics on thin-film lithium niobate," *Adv. Opt. Photonics* **13**(2), 242 (2021).
9. M. Zhang, C. Wang, P. Kharel, *et al.*, "Integrated lithium niobate electro-optic modulators: when performance meets scalability," *Optica* **8**(5), 652 (2021).
10. C. Wang, M. Zhang, B. Stern, *et al.*, "Nanophotonic lithium niobate electro-optic modulators," *Opt. Express* **26**(2), 1547–1555 (2018). Publisher: Optical Society of America.
11. M. Zhang, C. Wang, R. Cheng, *et al.*, "Monolithic ultra-high-Q lithium niobate microring resonator," *Optica* **4**(12), 1536 (2017).
12. Y. Gao, F. Lei, M. Girardi, *et al.*, "Compact lithium niobate microring resonators in the ultrahigh Q/V regime," *Opt. Lett.* **48**(15), 3949 (2023).
13. Y. Gao, Y. Sun, I. Rebolledo-Salgado, *et al.*, "Tightly-Confined and Long Z-Cut Lithium Niobate Waveguide with Ultralow-Loss," *Laser Photonics Rev.* **19**(21), e00042 (2025).
14. A. Boes, B. Corcoran, L. Chang, *et al.*, "Status and Potential of Lithium Niobate on Insulator (LNOI) for Photonic Integrated Circuits," *Laser Photonics Rev.* **12**(4), 1700256 (2018).
15. R. Zhuang, J. He, Y. Qi, *et al.*, "High- Q Thin-Film Lithium Niobate Microrings Fabricated with Wet Etching," *Adv. Mater.* **35**(3), 2208113 (2023).
16. Y. Tan, S. Niu, M. Billet, *et al.*, "Micro-transfer Printed Thin Film Lithium Niobate (TFLN)-on-Silicon Ring Modulator," *ACS Photonics* **11**(5), 1920–1927 (2024).
17. Z. Li, J. A. Smith, M. Scullion, *et al.*, "Photonic integration of lithium niobate micro-ring resonators onto silicon nitride waveguide chips by transfer-printing," *Opt. Mater. Express* **12**(11), 4375 (2022).
18. L. De Jaeger, T. Vandekerckhove, T. Reep, *et al.*, "Compact low-voltage lithium niobate racetrack modulator on a silicon nitride platform through micro-transfer printing," *Opt. Lett.* **50**(16), 4942 (2025).
19. M. Niels, E. Vissers, T. Vanackere, *et al.*, "Demonstration of lithium niobate integration on a 200-mm silicon photonics wafer using transfer printing," *Opt. Lett.* **50**(15), 4678 (2025).
20. L. Chen, M. G. Wood, and R. M. Reano, "125 pm/V hybrid silicon and lithium niobate optical microring resonator with integrated electrodes," *Opt. Express* **21**(22), 27003 (2013).
21. L. Chen, Q. Xu, M. G. Wood, *et al.*, "Hybrid silicon and lithium niobate electro-optical ring modulator," *Optica* **1**(2), 112 (2014).
22. A. N. R. Ahmed, S. Shi, M. Zablocki, *et al.*, "Tunable hybrid silicon nitride and thin-film lithium niobate electro-optic microresonator," *Opt. Lett.* **44**(3), 618 (2019).
23. S. Jin, L. Xu, H. Zhang, *et al.*, "LiNbO₃ Thin-Film Modulators Using Silicon Nitride Surface Ridge Waveguides," *IEEE Photonics Technol. Lett.* **28**(7), 736–739 (2016).
24. A. Rao, A. Patil, P. Rabiei, *et al.*, "High-performance and linear thin-film lithium niobate Mach-Zehnder modulators on silicon up to 50 GHz," *Opt. Lett.* **41**(24), 5700 (2016).
25. A. N. R. Ahmed, S. Shi, A. J. Mercante, *et al.*, "High-performance racetrack resonator in silicon nitride - thin film lithium niobate hybrid platform," *Opt. Express* **27**(21), 30741 (2019).
26. A. N. R. Ahmed, S. Nelan, S. Shi, *et al.*, "Subvolt electro-optical modulator on thin-film lithium niobate and silicon nitride hybrid platform," *Opt. Lett.* **45**(5), 1112 (2020).

27. Y. Wang, Z. Chen, L. Cai, *et al.*, “Amorphous silicon-lithium niobate thin film strip-loaded waveguides,” *Opt. Mater. Express* **7**(11), 4018 (2017).
28. L. Cao, A. Aboketaf, Z. Wang, *et al.*, “Hybrid amorphous silicon (a-Si:H)–LiNbO₃ electro-optic modulator,” *Opt. Commun.* **330**, 40–44 (2014).
29. S. Li, L. Cai, Y. Wang, *et al.*, “Waveguides consisting of single-crystal lithium niobate thin film and oxidized titanium stripe,” *Opt. Express* **23**(19), 24212 (2015).
30. T. Jin, J. Zhou, and P. T. Lin, “Mid-Infrared Electro-Optical Modulation Using Monolithically Integrated Titanium Dioxide on Lithium Niobate Optical Waveguides,” *Sci. Rep.* **9**(1), 15130 (2019).
31. A. Rao, A. Patil, J. Chiles, *et al.*, “Heterogeneous microring and Mach-Zehnder modulators based on lithium niobate and chalcogenide glasses on silicon,” *Opt. Express* **23**(17), 22746 (2015).
32. E. A. J. Marcatili, “Dielectric Rectangular Waveguide and Directional Coupler for Integrated Optics,” *Bell Syst. Tech. J.* **48**(7), 2071–2102 (1969).
33. Z. Yu, X. Xi, J. Ma, *et al.*, “Photonic integrated circuits with bound states in the continuum,” *Optica* **6**(10), 1342–1348 (2019). Publisher: Optica Publishing Group.
34. C. Zou, J. Cui, F. Sun, *et al.*, “Guiding light through optical bound states in the continuum for ultrahigh- *Q* microresonators,” *Laser Photonics Rev.* **9**(1), 114–119 (2015).
35. Z. Yu, Y. Tong, H. K. Tsang, *et al.*, “High-dimensional communication on etchless lithium niobate platform with photonic bound states in the continuum,” *Nat. Commun.* **11**(1), 2602 (2020).
36. T. G. Nguyen, G. Ren, S. Schoenhardt, *et al.*, “Ridge Resonance in Silicon Photonics Harnessing Bound States in the Continuum,” *Laser Photonics Rev.* **13**(10), 1900035 (2019).
37. M. A. Webster, R. M. Pafchek, A. Mitchell, *et al.*, “Width Dependence of Inherent TM-Mode Lateral Leakage Loss in Silicon-On-Insulator Ridge Waveguides,” *IEEE Photonics Technol. Lett.* **19**(6), 429–431 (2007).
38. T. G. Nguyen, A. Boes, and A. Mitchell, “Lateral Leakage in Silicon Photonics: Theory, Applications, and Future Directions,” *IEEE J. Sel. Top. Quantum Electron.* **26**(2), 1–13 (2020).
39. T. Vanackere, T. Vandekerckhove, L. Bogaert, *et al.*, “Heterogeneous integration of a high-speed lithium niobate modulator on silicon nitride using micro-transfer printing,” *APL Photonics* **8**(8), 086102 (2023).
40. Z. Yu, X. Xi, J. Ma, *et al.*, “Photonic integrated circuits with bound states in the continuum: erratum,” *Optica* **9**(7), 683 (2022).
41. Flexcompute Inc. <https://flexcompute.com> (2025). (accessed: 2025-08-14).
42. F. Vogelbacher, S. Nevlacsil, M. Sagmeister, *et al.*, “Analysis of silicon nitride partial Euler waveguide bends,” *Opt. Express* **27**(22), 31394 (2019).